Tornado-Scale Vortices in the Tropical Cyclone Boundary Layer: Numerical Simulation with WRF-LES Framework

Liguang Wu[1,2], Qingyuan Liu[1] and Yubing Li[1]

[1]Pacific Typhoon Research Center and Key Laboratory of Meteorological Disaster of Ministry of Education, Nanjing University of Information Science and Technology, Nanjing, China

[2]Department of Atmospheric and Oceanic Sciences and Institute of Atmospheric Sciences, Fudan University, Shanghai, China

December 20, 2018

Revised for *Atmos. Chem. Phys.*

Corresponding author address: Dr. Liguang Wu

Pacific Typhoon Research Center

Nanjing University of Information Science and Technology, Nanjing, Jiangsu 210044

E-mail: liguang@nuist.edu.cn

Abstract

The tornado-scale vortex in the tropical cyclone (TC) boundary layer (TCBL) has been observed in intense hurricanes and the associated intense turbulence poses a severe threat to the manned research aircraft when it penetrates hurricane eyewalls at a lower altitude. In this study, a numerical experiment in which a TC evolves in a large-scale background over the western North Pacific is conducted using the Advanced Weather Research and Forecast (WRF) model by incorporating the large eddy simulation (LES) technique. The simulated tornado-scale vortex shows features similar to those revealed with limited observational data, including the updraft/downdraft couplet, the sudden jump of wind speeds, the location along the inner edge of the eyewall, and the small horizontal scale. It is suggested that the WRF-LES framework can successfully simulate the tornado-scale vortex with the grids at the resolution of 37 m that cover the TC eye and eyewall.

The simulated tornado-scale vortex is a cyclonic circulation with a small horizontal scale of ~1 km in the TCBL. It is accompanied by strong updrafts (more than 15 m s^{-1}) and large vertical components of relative vorticity (larger than 0.2 s^{-1}). The tornado-scale vortex favorably occurs at the inner edge of the enhanced eyewall convection or rainband within the saturated, high-θ_e layer, mostly below the altitude of 2 km. Nearly in all the simulated tornado-scale vortices, the narrow intense updraft is coupled with the relatively broad downdraft, constituting one or two updraft/downdraft couplets or horizontal rolling vortices, as observed by the research aircraft. The presence of the tornado-scale vortex also leads to significant gradients in the near surface wind speed and wind gusts.

1. Introduction

Tropical cyclones (TCs) pose a severe risk to life and property in TC-prone areas and the risk will increase due to the rapidly rising coastal population and buildings (Pielke et al. 2008; Zhang et al. 2009). One of the major TC threats is damaging winds. Uneven damage patterns often show horizontal scales ranging from a few hundred meters to several kilometers (Wakimoto and Black 1994; Wurman and Kosiba 2018), suggesting that TC threats are associated with both sustained winds and gusts. The latter are believed to result from small-scale coherent structures in the TC boundary layer (Wurman and Winslow 1998; Morrison et al. 2005; Lorsolo et al. 2008; Kosiba et al. 2013; Kosiba and Wurman 2014). The small-scale coherent structures may have significant implications for the vertical transport of energy in TCs and thus TC intensity and structure (Zhu 2008; Rotunno et al. 2009; Zhu et al. 2013; Green and Zhang 2014, 2015; Gao et al. 2017). While understanding of the coherent structure is very important for mitigating TC damage and understanding of TC intensity and structure changes, for now direct in situ observation and remote sensing measurements can only provide very limited information.

In the TC boundary layer (TCBL), observational analyses suggest that horizontal streamwise roll vortices prevail with sub-kilometer to multi-kilometer wavelengths (Wurman and Winslow 1998; Katsaros et al. 2002; Morrison et al. 2005; Lorsolo et al. 2008; Ellis and Businger 2010; Foster, 2013). Studies found that the rolls can result from the inflection point instability of the horizontal wind profiles in the TCBL (Foster 2005; Gao and Ginis 2014) and have significant influences on the vertical transport of energy in TCs (Zhu 2008; Rotunno et al. 2009; Zhu et al. 2013; Green and Zhang 2014, 2015; Gao et al. 2017). The TCBL is known to play a critical role in transporting energy and

77 controlling TC intensity (Braun and Tao 2000; Rotunno et al. 2009; Smith and
78 Montgomery 2010; Bryan 2012; Zhu et al. 2013; Green and Zhang 2015).

79 Another important small-scale feature is the so-called eyewall vorticity maximum
80 (EVM) (Marks et al. 2008) or tornado-scale vortices in the TCBL (Wurman and Kosiba
81 2018; Wu et al. 2018). So far, our understanding is mainly from a few observational
82 analyses based on limited data collected during the research aircraft penetration of
83 hurricane eyewalls. A WP-3D research aircraft from National Oceanic and Atmospheric
84 Administration (NOAA) encountered three strong updraft-downdraft couplets within one
85 minute while penetrating the eyewall of category 5 Hurricane Hugo (1989) at 450-m
86 altitude (Marks et al. 2008). The severe turbulence caused the failure of one of the four
87 engines and the people aboard were at a severe risk. The aircraft finally escaped with the
88 help of a U. S. Air Force reconnaissance WC-130 aircraft, which found a safe way out
89 through the eyewall on the northeast side of Hugo. Since then the aircraft mission has
90 been prohibited in the boundary layer of the TC eyewall. Later analysis indicated that the
91 dangerous turbulence was associated with a tornado-scale vortex, which is comparable to
92 a weak tornado in terms of its diameter of about 1 km and the estimated peak cyclonic
93 vorticity of 0.125 s^{-1} (Marks et al. 2008). Such strong turbulence was also observed in
94 Hurricanes Isabel (2003) and Felix (2007) below 3 km (Aberson et al. 2006; Aberson et
95 al. 2017). So far, little is known about the structure and evolution of the tornado-scale
96 vortex.

97 With advances in numerical models and computational capability, the large eddy
98 simulation (LES) technique has been incorporated into the Advanced Weather Research
99 and Forecast (WRF) model (Mirocha et al. 2010) and an increasing number of TC

simulations have been conducted with horizontal grid spacing less than 1 km (Zhu 2008; Rotunno et al. 2009; Bryan et al. 2014; Stern and Bryan 2014; Rotunno and Bryan 2014; Green and Zhang 2015). In LES, the energy-producing scales of 3-dimensional (3D) atmospheric turbulence in the planetary boundary layer (PBL) are explicitly resolved, while the smaller-scale portion of the turbulence is parameterized (Mirocha et al. 2010). Effort has been made to simulate the structure of the TC PBL eddies and the associated influence on TC intensity. Zhu (2008) simulated the structure of the coherent large eddy circulations and the induced vertical transport using the WRF-LES framework with horizontal resolutions of 300 m and 100 m. When the horizontal resolution was increased from 185 to 62 m on the *f*-plane, Rotunno et al. (2009) found a sharp increase in randomly distributed small-scale turbulent eddies, while 1-minute mean TC intensity began to decrease. Green and Zhang (2015) performed several 6-hour one-way simulations of Hurricane Katrina (2005) without a boundary layer parameterization (horizontal resolutions of 333, 200, and 111 m). Rotunno et al. (2009) and Green and Zhang (2015) suggest that the horizontal resolution should be below 100 m to simulate the development of 3D turbulent eddies in TCBL. Ito et al. (2017) found that the near-surface coherent structures can be successfully simulated by using the horizontal resolution of 70 m, which appear to be caused by an inflection-point instability of both radial and tangential winds.

It is clear that understanding of the tornado-scale vortex would enhance the safety of flights into very intense TCs. In addition, the tornado-scale vortex may contribute to TC intensification by mixing the high-entropy air in the eye into the eyewall (Persing and Montgomery 2003; Montgomery et al. 2006; Aberson et al. 2006) and track fluctuations

(Marks et al. 2008; Aberson et al. 2017). By simulating the tornado-scale vortex in the TCBL, this study will particularly focus on the spatial distribution of the occurrence of the tornado-scale vortex and the features of its 3D structures.

2. The numerical experiment

In this study the numerical simulation is conducted using version 3.2.1 of the WRF model. Following Wu and Chen (2016), two steps were taken to construct the initial conditions for the numerical experiment. A symmetric vortex was first spun up without the environmental flow on an *f*-plane for 18 hours and then the vortex was embedded in the large-scale background of Typhoon Matsa (2005) from 0000 UTC 5 August to 1200 UTC 6 August. The large-scale environment was derived from the National Centers for Environmental Prediction (NCEP) Final (FNL) Operational Global Analysis data with resolution of 1.0° × 1.0° using a 20-day low-pass Lanczos filter (Duchon 1979).

The spun-up vortex is initially located at the center of Typhoon Matsa (25.4°N, 123.0°E). The outermost domain centered at 30.0°N, 132.5°E covers an area of 6210×6210 km with a horizontal grid spacing of 27 km. The numerical experiment is designed with six two-way interactive domains embedded in the 27-km resolution domain to simulate energetic 3-dimensional turbulent eddies in the TC eyewall and their influence on the TC vortex, mesoscale rainbands and convective clouds. The horizontal spacing decreases by a factor of 3 with the domain level. The corresponding horizontal resolutions are 9 km, 3 km, 1 km, 1/3 km (333 m), 1/9 km (~111 m) and 1/27 km (~37 m) and the numbers of their grid meshes are 230×210, 432×399, 333×333, 501×501, 1351×1351, and 2431×2431, respectively. The innermost domain covers the inner region of the simulated TC (90×90 km^2), including the eye and eyewall. Except for the 27-km

146 and 9-km resolution domains, the other domains move with the TC. The model consists
147 of 75 vertical levels (19 levels below 2 km) with a top of 50 hPa and is run over the open
148 ocean with a constant sea surface temperature of 29ºC.

149 The physics options used in the simulation are as follows. The Kain-Fritsch cumulus
150 parameterization scheme and the WRF single-moment 3-class scheme are used in the
151 outermost domain (Kain and Fritsch 1993). The WRF 6-class scheme is selected in the
152 nested domains with no cumulus parameterization scheme (Hong and Lim 2006). The
153 Rapid Radiative Transfer Model (RRTM) and the Dudhia shortwave radiation scheme are
154 used for calculating long-wave radiation and shortwave radiation (Mlawer et al. 1997;
155 Dudhia 1989). The LES technique is used in the sub-kilometer domains (Mirocha et al.
156 2010) and the Yonsei University scheme is adopted for PBL parameterization in the other
157 domains (Noh et al. 2003).

158 The model is run for 36 hours and the 1/9-km-resolution and 1/27-km-resolution
159 domains are activated at 24 h. In the following analysis, we will focus on the hourly
160 output from 26 h to 36 h. The TC center is determined with a variational approach in
161 which it is located until the maximum azimuthal-mean tangential wind speed is obtained
162 (Wu et al. 2006).

163 **3. The simulated small-scale features**

164 The simulated TC takes a north northwest track (figure not shown). Figure 1 shows
165 its intensity in terms of the maximum instantaneous and azimuthally averaged wind
166 speeds at 10 m in the 1/27 km-resolution domain. The instantaneous winds are obtained
167 directly from the model output without any time averaging. The azimuthal wind speed is
168 the wind speed averaged azimuthally with respect to the TC center. The instantaneous

maximum wind speed fluctuates between 61.8 m s^{-1} and 76.6 m s^{-1} during the 12-hour period, while the fluctuations in the azimuthal maximum wind speed is relatively small, ranging from 43.5 m s^{-1} to 48.8 m s^{-1}. In particular, the TC maintains the azimuthal mean maximum wind speed of ~45 m s^{-1} after the innermost domain has been activated for two hours.

Figure 2a shows the simulated 500-m radar reflectivity at 27 h, indicating that the eyewall is open to the south of the TC center. We examine the radar reflectivity field and find that the opened eyewall persists during the 11-hour period (figure not shown). In addition, the location of the enhanced convection relative to the TC center is generally steady. It is well known that the eyewall asymmetry is associated with the vertical shear of the environmental flow (Frank and Ritchie 2001, Braun and Wu 2007). In this study the vertical wind shear is calculated as the difference of wind vectors between 200 hPa and 850 hPa within a radius of 300 km. As shown in the figure, the mean shear is 7.0 m s^{-1} to the southeast over the 11-hour period. In agreement with the previous studies, the enhanced eyewall reflectivity is generally observed in the downshear left side. There are relatively small changes in the RMW during the 11-hour period, ranging from 28.2 km to 30.7 km at 500 m.

Using the fine-scale dual Doppler data in the right front quadrant and eye of Hurricane Frances (2004) as it made landfall on Florida, Kosiba and Wurman (2014) found linear coherent structures with a wavelength of 400-500 m near the surface. Figure 2b shows the simulated near-surface (10 m) wind speeds in the inner region at 27 h. The instantaneous wind speed is dominated by quasi-linear coherent structures in the eyewall region. The intense instantaneous wind speeds coincide with the TC-scale shear-induced

192 enhanced eyewall convection shown in Figure 2a. In order to show clearly the quasi-
193 linear feature, we plot the instantaneous wind speed in an area of 7×10 km^2 at this time
194 (Fig. 3a). The small area is located in the eyewall to the east of the TC center (Fig. 2b).
195 The streaks of alternating high and low wind speeds can be clearly seen, which are
196 roughly aligned with the TC-scale flow with an outward angle. We can see that the
197 instantaneous wind speed exhibits large gradients across the quasi-linear structures.

198 Figure 3b shows the perturbation wind field at 500 m in the small area. The
199 perturbation winds are obtained by subtracting an 8-km moving mean. We compare the
200 perturbation winds with different sizes of the moving window. While the perturbation
201 wind fields are very similar, the wind speeds generally increase with the increasing
202 window size. When the window size is larger than 8 km, there is little change in the
203 perturbation wind speed. The simulated small-scale circulations are similar to those by
204 subtracting the symmetric and wavenumber 1-3 components with respect to the TC center.
205 In the perturbation wind field, we can see two small-scale cyclonic circulations. The most
206 distinct one has a diameter of ~2 km. In the next section, the two cyclones are identified
207 as two tornado-scale vortices (M2701 and M2705). In the study, the simulated tornado-
208 scale vortex is named with four digits. While the first two digits indicate the hours of the
209 simulation, the last two digits is the series number at the same hour. Compared to Figure
210 3a, the two tornado-scale vortices also correspond to enhanced wind speeds at 10 m.

211 **4. Identification of TSVs**

212 As mentioned in Section 1, analyses of a few real cases in Atlantic intense hurricanes
213 indicate that the tornado-scale vortex is a small-scale feature that occurs in the turbulent
214 TC boundary, with vertical motion and relative vorticity extremes. Aberson et al. (2006)

and Aberson et al. (2017) analyzed the extreme updrafts in Hurricanes Isabel (2003) and Felix (2007) and suggested that the strong updrafts were likely associated with the small scale vortex. The updraft of 25 m s^{-1} in Isabel was detected by a GPS dropwindsonde just below 800 hPa, while the updraft of 31 m s^{-1} in Hurricane Felix (2007) was observed at the flight altitude (~ 3 km). Marks et al. (2008) found that the EVM in Hurricane Hugo (1989) was associated with a maximum vertical motion of 21 m s^{-1} and a maximum vertical relative vorticity of 0.125 s^{-1} at the altitude of 450 m. Based on these studies, a small scale vortex associated with extreme wind speed can be treat as tornado-scale vortex (Wurman and Kosiba 2018; Wu et al. 2018). The tornado-scale vortex in the simulated TC is subjectively defined as a small-scale cyclonic circulation with the diameter of 1-2 km below the altitude of 3 km, containing maximum upward motion larger than 20 m s^{-1} and maximum vertical relative vorticity larger than 0.2 s^{-1}. The grid points that satisfy the thresholds of vertical motion and vertical relative vorticity belong to the same tornado-scale vortex if they are within a distance of 1 km in the horizontal or vertical direction. We detect the tornado-scale vortices using the output at one-hour intervals from 26 h to 36 h. A few variables are also stored at 3-second intervals during a 22-minute period from the 30 h.

There are 24 tornado-scale vortices identified in the 11-hour output (Table 1). There are four tornado-scale vortices with the maximum vertical motion more than 30 m s^{-1} and the maximum vertical component of relative vorticity larger than 0.4 s^{-1}. Except for the two tornado-scale vortices at 36 h, the others occur during 26 h-31 h with 10 cases at 27 h. The lull period is coincident with relatively weaker instantaneous maximum wind speed at 10 m although there is little difference in the azimuthal mean maximum wind speed

(Fig. 1). Examination indicates that the 10-m instantaneous wind speed maximum at 27 h is associated with M2701. It is suggested that the tornado-scale vortex can lead to the strongest wind gust in a TC.

Some previous studies argued that the presence of mesovortices intensifies the TC by mixing the high-entropy air in the eye into the eyewall (Persing and Montgomery 2003; Montgomery et al. 2006; Aberson et al. 2006). As shown in Figure 1, the azimuthal-mean maximum wind speed does not show any jump at 27 h, when there are 10 identified tornado-scale vortices. In the following discussion, we will show that the mixing indeed exists, but its effect on the azimuthal maximum wind speed cannot be detected. It is similar with the conclusion from idealized numerical experiments conducted by Bryan and Rotunno (2009). In fact, the azimuthal maximum wind speed (~45 m s^{-1}) is rather steady during the 11-hour period after the innermost domain has been activated for two hours.

The number of the identified tornado-scale vortices is sensitive to the threshold of vertical motion. If we relax the threshold of maximum vertical motion to 15 m s^{-1}, we can identify 89 tornado-scale vortices during the 11-hour period (Fig. 4a). Nearly all the tornado-scale vortices still occur in the same semicircle of the enhanced eyewall reflectivity. This relationship between the vertical wind shear orientation and the spatial distribution of extreme updrafts is consistent with what Stern et al. (2016) found from dropsonde observations in many storms. In our experiment, a few variables are also stored at 3-second intervals during a 22-minute period from the 30th hour. The duration of the tornado-scale vortex is examined in the 3-second output. The duration is counted as the continuous period during which the maximum vertical motion and vertical relative

vorticity are not less than the thresholds. For the thresholds of 20 m s^{-1} in vertical motion and 0.2 s^{-1} in vertical relative vorticity, the mean duration is 40 seconds and the longest is 138 seconds. We can conclude that the identified tornado-scale vortices are not repeatedly counted in the 1-hour output. Besides, the durations of tornado-scale vortices are consistent with the observational and numerical studies (Wurman and Kosiba 2018; Stern and Bryan 2018).

5. Spatial distribution of tornado-scale vortices

Figure 4a shows the location of the maximum vertical motions of the detected tornado-scale vortices including 89 vortices identified with the threshold of maximum vertical motion of 15 m s^{-1}. Different criteria give similar distribution pattern of tornado-scale vortices, thus we just discuss the 24 tornado-scale vortices defined under the threshold of maximum vertical motion of 20 m s^{-1} in the following discussion. The tornado-scale vortices exclusively occur in the semicircle with intense convection from the east to the northwest (Fig. 2a). Nearly all of the identified cases occur in the inward side of the radius of maximum wind (RMW) or close to the RMW (e.g., Stern et al. 2016; Stern and Bryan 2018), with two exceptions that are located outside of the RMW (Fig. 4a). One is M2901, which is 11.8 km from the RMW, and the other is M3601 being 7.3 km from the RMW (Table 1). Close examination indicates that the two tornado-scale vortices occur between two high reflectivity bands (figure not shown).

Although the real tornado-scale vortices were observed by chance, they were also associated with the intense radar reflectivity within the hurricane eyewall and sharp horizontal reflectivity gradients (Aberson et al. 2006, Marks et al. 2008 and Aberson et al. 2016). In agreement with these studies, all of the simulated tornado-scale vortices are

associated with sharp horizontal reflectivity gradients and most of them occur in the inner edge of the intense eyewall convection within the RMW. As shown in Figure 2a, all of the 10 cases at 27 h are located in the inner edge of the intense reflectivity. It is suggested that the tornado-scale vortex favorably occurs at the inner edge of the intense eyewall convection.

The gradient Richardson number (Ri) has largely been used as a criterion for assessing the stability of stratified shear flow. It is defined by

$$R_i = \frac{N^2}{S^2} \quad (1)$$

where $N^2 = g\frac{\partial \ln \theta_e}{\partial z}$ is the square of Brunt–Väisälä frequency, $S^2 = (\frac{\partial u}{\partial z})^2 + (\frac{\partial v}{\partial z})^2$ is the square of vertical shear of the horizontal velocity, g is the gravity acceleration, θ_e is the equivalent potential temperature, u is the zonal wind speed, and v is the meridional wind speed. z is the vertical coordinate. Using the smoothed fields, we also calculate the Richardson number for each tornado-scale vortex (Table 1). It is calculated at each level and then averaged over a layer between 200 m and 800 m within a radius of 1.5 km from the location of the maximum vertical motion. The Richardson number is small, and it is negative for seven cases. As suggested by Stern et al. (2016), the strong updraft is mainly within a kilometer of the surface and it is implausible for buoyancy to be the primary mechanism for vertical acceleration. In Figure 4a, the Richardson number is also plotted, which is averaged over the 11-hour period. We can see that the tornado-scale vortices generally occur in the areas with the Richardson number less than 0.25. It is indicated that the flow in these areas is dynamically unstable and turbulent. The areas coincide with the semicircle of the enhanced eyewall convection. Figure 4b further shows the field

306 of the Richardson number at 27 h. The 10 tornado-scale vortices are all in an environment
307 with the Richardson number less than 0.1. Since the Richardson number is calculated as
308 the ratio of the moist static stability to the vertical wind shear in the TCBL, we speculate
309 that the strong vertical wind shear in the inward side of the intense eyewall convection is
310 an important factor for the development of tornado-scale vortices.

311 Figure 5 shows the vertical cross sections of tangential wind, radial wind, vertical
312 motion, reflectivity and vertical relative vorticity below 2.5 km, which are averaged in
313 the northeast quadrant over the 11-hour period. Note that the radial locations of M2901
314 and M3601 are not shown in Figure 5 due to the effect of the limited innermost domain
315 on the calculation of the azimuthal mean. Note that there are relatively small changes in
316 the RMW during the 11-hour period. The maximum vertical motions associated with the
317 tornado-scale vortices are located inside the tilted RMW between the altitudes of 300 m
318 and 1300 m. Most of them (71%) are found between 400 m and 600 m. The height of the
319 maximum vertical motions becomes higher when the inflow layer deepens outward.
320 Figures 5b and 5c further indicate that the tornado-scale vortices are generally found in
321 the region of strong vertical motion averaged over the northeastern quadrant, where the
322 vortices are detected, and large vertical relative vorticity with sharp horizontal reflectivity
323 gradient on the inward side of the eyewall.

324 **6. Tornado-scale vortex structure**

325 Using the high-resolution model output, we can explore the structural features of the
326 simulated tornado-scale vortex. After examination of all of the identified 24 tornado-scale
327 vortices, we find that they can be classified into three categories based on its vertical

328 structure, especially in terms of its vertical extension, stratification and near-surface wind
329 jump.

330 The first category includes 17 cases, accounting for 71% of the total. Their structural
331 features can be represented by M2701, one of the four strongest tornado-scale vortices,
332 located 4.3 kilometers inward from the 500-m RMW (Table 1). In fact, the four strongest
333 belong to the same category. In this category, nearly all of the maximum vertical motions
334 occur around the altitude of 500 m, except M3001. The maximum vertical motion of
335 M2701 is 31.98 m s^{-1} at the altitude of 400 m, while the maximum vertical relative
336 vorticity of 0.55 s^{-1} occurs at 200 m (Table 1). The 3D structure of the tornado-scale
337 vortex can be clearly demonstrated by the streamlines of perturbation winds near the
338 strong updraft (Fig. 6). The flows curl cyclonically upward from the surface (Fig. 6a).
339 The tornado-scale vortex is manifested by a small-scale circulation extending upward to
340 ~1.5 km. In addition, the tornado-scale vortex is closely associated with
341 updraft/downdraft couplets (Fig. 6b). Fig. 6c shows that the tornado-scale vortex is a
342 complex twisted vortex system. The system has strong horizontal circulation below 1-km
343 and it turns into vertical circulation as the height increases. So it contains both strong
344 horizontal and vertical circulations.

345 Figure 7 shows the vertical cross section of vertical motion, equivalent potential
346 temperature, and simulated radar reflectivity along the line in Figure 3b for M2701. The
347 inflow from the outward side and the outflow from the eye side converge near the surface
348 to the strong updraft that is below ~1.5 km. The updraft and the downward motion to its
349 radially outward flank constitute a horizontal rolling vortex. On the top of the updraft,
350 there is a layer of the high equivalent potential temperature (θ_e) layer (Fig. 7b). To the

351 eye side of the updraft, there is a high θ_e layer below ~1.5 km. The high θ_e layer tilts
352 upward and extends outward. The large radar reflectivity can be found below the high θ_e
353 layer (Fig. 7c). The intense updraft is located in the inner edge of the large radar
354 reflectivity region. In addition, as suggested by Aberson et al. (2006) and Marks et al.
355 (2008), the strong updraft is within a saturated layer (Fig. 8a), coinciding with high
356 vertical relative vorticity (Fig. 8c).

357 To the right of the updraft (Fig. 7b), another high θ_e layer can be seen at the altitude
358 of ~500 m. We check other cases in this category of vortices and find that the lower-
359 altitude high θ_e layer is not always present. The downward motion at ~500 m may be
360 responsible for the lower-altitude high θ_e layer. The relatively low θ_e near the surface
361 corresponds to the inflow layer. The high θ_e air meets with the cold inflow air, resulting
362 in relatively lower θ_e in the strong updraft. It is indicated that the high θ_e air in the eye is
363 locally entrained into the TC eyewall.

364 Some previous studies have shown that the quasi-linear bands are closely associated
365 with the horizontal rolls in the TC boundary layer due to the upward and downward
366 momentum transports (Wurman and Winslow 1998; Katsaros et al. 2002; Morrison et al.
367 2005; Lorsolo et al. 2008; Ellis and Businger 2010; Foster 2013). To demonstrate the
368 relationship, Figure 8b shows the cross section of winds along the line shown in Figure
369 3b and the corresponding wind speeds at 10 m and 400 m. The figure clearly shows that
370 the wind speed fluctuations at 10 m are associated with the changes of the vertical
371 motions in Fig. 7a. The wind speed jump (Fig. 8b) is significant across the intense updraft
372 (Fig. 7a). At 10 m, the wind speed suddenly increases from ~30 m s^{-1} to ~60 m s^{-1}. Note
373 that the wind speed jump is larger at 400 m, ranging from ~35 m s^{-1} to ~95 m s^{-1}. Marks

et al. (2008) reported that the wind speed at 450-m altitude increased rapidly from <40 m s^{-1} to 89 m s^{-1} in the Hurricane Hugo (1989) when the NOAA research aircraft encountered an EVM. We argue that the superposition of the horizontal cyclonic circulation of the tornado-scale vortices plays an important role in enhancing wind gusts on its radially outward side.

There are three tornado-scale vortices in the second category, including M2706, M2707 and M2708. The structural features can be represented by M2708. In M2708, the maximum vertical motion and vertical relative vorticity occur at 900 m and 800 m, respectively (Table 1). The vertical motion of more than 12 m s^{-1} extends vertically from the near surface to ~2 km (Fig. 9a). In this category, we cannot see the warm air with high θ_e (Fig. 9b) and the strong updraft is located in a statically unstable stratification (Table 1). The wind speed at the altitude of 900 m varies by ~20 m s^{-1} across the updraft, while the wind speed gradient is relatively weak at 10 m (Fig. 9c).

The third category includes four cases: M2600, M2703, M2705 and M3002, in which the updraft occurs in a statically stable stratification (Table 1). Here we use M3002 as an example to show its vertical structure. As shown in Fig. 10a, the updraft is elevated between 0.5 km and 2 km. The maximum vertical motion and relative vorticity are found at the altitude of 1300 m. In this category, a pronounced feature is the deep low θ_e (less than 364 K) layer in the inflow layer (Fig. 10b). As shown in Figure 10c, the gradient of the wind speed at 10 m is not clear while there is a speed jump of ~30 m s^{-1} in the vicinity of the updraft at 1300 m.

Previous studies suggest that the horizontal resolution should be below 100 m to simulate the development of 3D turbulent eddies in TCBL (Rotunno et al. 2009; Green and Zhang 2015). Based on our numerical experiment, the tornado-scale vortex can be successfully simulated with the grids at the resolution of 37 m. It should be noted that we have 12 vertical levels below 1km.Vertical resolution in the innermost domain seems to be relatively coarse compared to the horizontal spacing of 37 m. We also conducted the an experiment with the innermost domain resolution of 111 m. In the experiment, the vertical resolution and horizontal resolution are comparable in TC boundary layer. The tornado-scale vortices can also be found in the experiment. At this time, we are not sure that the three categories represent different phases in the life cycle of these coherent structures, since the 3-second output does not contain the thermodynamic variables, we cannot examine the hydrostatic stratification.

7. Summary

The tornado-scale vortex or EVM in the TCBL has been observed in intense hurricanes and is always associated with strong turbulence. To understand the complicated interactions of the large-scale background flow, TC vortex, mesoscale organization, down to fine-scale turbulent eddies, a numerical experiment in which a TC evolves in a typical large-scale background over the western North Pacific is conducted using the WRF-LES framework with six nested grids. The simulated tornado-scale vortex shows features similar to those revealed with limited observations. It is suggested that the WRF-LES framework can successfully simulate the tornado-scale vortex with the grids at the resolution of 37 m that cover the TC eye and eyewall.

Following Wu et al. (2018), the tornado-scale vortex can be defined as a small-scale cyclonic circulation with the maximum vertical motion not less than 20 m s^{-1} and maximum vertical relative vorticity not less than 0.2 s^{-1}. A total of 24 tornado-scale vortices can be identified in the 11-hour output. Nearly all of them are within or close to the RMW. Most of them occur in the inward side of the intense eyewall convection, mostly below the altitude of 2 km. Tornado-scale vortices are mostly in neutral or stable stratification within the saturated, high-θ_e layer. The tornado-scale vortex generally occurs in the areas with the Richardson number less than 0.25. We speculate that the strong vertical wind shear in the inward side of the intense eyewall convection is an important factor for the development of tornado-scale vortices.

The simulated tornado-scale vortex has a small horizontal scale of 1-2 km in the TCBL. It is accompanied by strong updrafts (more than 20 m s^{-1}) and a cyclonic circulation with large vertical components of relative vorticity (larger than 0.2 s^{-1}). The tornado-scale vortex is closely associated with horizontal rolls. Nearly in all of the simulated tornado-scale vortex cases, the narrow intense updraft is coupled with the relatively broad downdraft (figures not shown), constituting an updraft/downdraft couplet or horizontal rolling vortex, as observed by the research aircraft. Since the tornado-scale vortex is associated with intense updrafts and strong wind gusts, its presence can pose a severe threat to the eyewall penetration of manned research aircraft and the strong wind gusts associated with tornado-scale vortices can pose a severe risk to coastal life and property.

Acknowledgments. We thank Prof. Ping Zhu of Florida International University for aiding with the WRF-LES framework. This research was jointly supported by the

National Basic Research Program of China (2015CB452803), the National Natural Science Foundation of China (41730961, 41675051, 41675009), and Jiangsu Provincial Natural Science Fund Project (BK20150910). The numerical simulation was carried out on the Tianhe Supercomputer, China.

References

Aberson, S. D., Black, M., Montgomery, M. T. and Bell, M.: Hurricane Isabel (2003): New Insights Into the Physics of Intense Storms. Part II: Extreme Localized Wind, *Bull. Amer. Meteor. Soc.*, **87**, 2006.

Aberson, S. D., Zhang, J. A. and Ocasio, K. N.: An Extreme Event in the Eyewall of Hurricane Felix on 2 September 2007, *Mon. Wea. Rev.*, **145**, 2017.

Braun, S. A. and Tao, W.-K.: Sensitivity of High-Resolution Simulations of Hurricane Bob (1991) to Planetary Boundary Layer Parameterizations. *Monthly Weather Review*, **128**, 3941–3961, 2000.

Braun, S. A. and Wu, L.: A Numerical Study of Hurricane Erin (2001). Part II: Shear and the Organization of Eyewall Vertical Motion. *Monthly Weather Review*, **135**, 1179–1194, 2007.

Bryan, G. H., and R. Rotunno: The influence of near-surface, high-entropy air in hurricane eyes on maximum hurricane intensity. *J. Atmos. Sci.*, **66**, 148–158, 2009.

Bryan, G. H.: Effects of surface exchange coefficients and turbulence length scales on the intensity and structure of numerically simulated hurricanes. *Mon. Wea. Rev.*, **140**, 1125–1143, 2012.

Bryan, G. H., Stern, D. P., and Rotunno, R.: A Framework for Studying the Inner Core of Tropical Cyclones Using Large Eddy Simulation, paper presented at 31st Conference on Hurricanes and Tropical Meteorology, *Am. Meteorol. Soc.*, San Diego, Calif, 2014.

Duchon, C. E.: Lanczos filtering in one and two dimensions. *J. Appl. Meteor.*, **18**, 1016–1022, 1979.

Dudhia, J.: Numerical study of convection observed during the winter monsoon experiment using a mesoscale two-dimensional model. *J. Atmos. Sci.*, **46**, 3077-3107, 1989.

Ellis, R. and Businger, S.: Helical Circulations in the Typhoon Boundary Layer. *Journal of Geophysical Research*, **115**, D06205, 2010.

Foster, R.: Why rolls are prevalent in the hurricane boundary layer. *Journal of the atmospheric sciences*, **62**, 2647–2661, 2005.

Foster, R.: Signature of Large Aspect Ratio Roll Vortices in Synthetic Aperture Radar Images of Tropical Cyclones. *Oceanography*, **26**, 58-67, 2013.

Frank, W. M. and Ritchie, E. A.: Effects of vertical wind shear on the intensity and structure of numerically simulated hurricanes. *Mon. Wea. Rev.*, **129**, 2249-2269, 2001.

Gao, K. and Ginis, I.: On the Generation of Roll Vortices due to the Inflection Point Instability of the Hurricane Boundary Layer Flow. *Journal of the Atmospheric Sciences*, **71**, 4292–4307, 2014.

Gao, K., Ginis, I., Doyle, J. D. and Jin, Y.: Effect of Boundary Layer Roll Vortices on the Development of an Axisymmetric Tropical Cyclone. *Journal of the Atmospheric Sciences*, **74**, 2737–2759, 2017.

Green, B. W. and Zhang, F.: Sensitivity of Tropical Cyclone Simulations to Parametric Uncertainties in Air–Sea Fluxes and Implications for Parameter Estimation. *Monthly Weather Review*, **142**, 2290–2308, 2014.

Green, B. W. and Zhang, F.: Numerical simulations of Hurricane Katrina (2005) in the turbulent gray zone, *Journal of Advances in Modeling Earth Systems*, **7**, 142–161, 2015.

Hong, S.–Y. and Lim, J.–O. J.: The WRF single–moment 6–class microphysics scheme (WSM6). *J. Korean Meteor. Soc.*, **42**, 129–151, 2006.

Ito, J., Oizumi T., and Niino H.: Near-surface coherent structures explored by large eddy simulation of entire tropical cyclones. *Sci. Rep.*, **7**, 3798, 2017.

Kain, J. S. and Fritch, J. M.: Convective parameterization for mesoscale models: The Kain–Fritch scheme. *The Representation of Cumulus Convection in Numerical Models*, Meteor. Monogr., Amer. Meteor. Soc., **46**, 165–170, 1993.

Kosiba, K., Wurman, J., Masters, F. J., and Robinson, P.: Mapping of Near-Surface Winds in Hurricane Rita Using Finescale Radar, Anemometer, and Land-Use Data. *Monthly Weather Review*, **141**, 4337–4349, 2013.

Kosiba, K. A. and Wurman, J.: Finescale Dual-Doppler Analysis of Hurricane Boundary Layer Structures in Hurricane Frances (2004) at Landfall. *Monthly Weather Review*, **142**, 1874–1891, 2014.

Lorsolo, S., Schroeder, J. L., Dodge, P., and Marks, F.: An Observational Study of Hurricane Boundary Layer Small-Scale Coherent Structures. *Monthly Weather Review*, **136**, 2871–2893, 2008.

Marks, F. D., Black, P. G., Montgomery, M. T., and Burpee, R. W.: Structure of the Eye and Eyewall of Hurricane Hugo (1989). *Monthly Weather Review*, **136**, 1237–1259,2008.

Mirocha, J. D., Lundquist, J. K., and Kosović, B.: Implementation of a Nonlinear Subfilter Turbulence Stress Model for Large-Eddy Simulation in the Advanced Research WRF Model. *Monthly Weather Review*, **138**, 4212–4228, 2010.

Mlawer, E. J., Taubman, S. J., Brown, P. D., Iacono, M. J., and Clough, S. A.: Radiative transfer for inhomogeneous atmosphere: RRTM, a validated correlated-k model for the longwave. *J. Geophys. Res.*, **102 (D14)**, 16663–16682, 1997.

Montgomery, M. T., Bell, M. M., Aberson, S. D., and Black, M. L.: Hurricane Isabel (2003): New Insights into the Physics of Intense Storms. Part I: Mean Vortex Structure and Maximum Intensity Estimates. *Bull. Amer. Meteor. Soc.*, **87**, 1335–1347, 2006.

Morrison, I., Businger, S., Marks, F., Dodge, P., and Businger, J. A.: An Observational Case for the Prevalence of Roll Vortices in the Hurricane Boundary Layer. *Journal of the atmospheric sciences*, **62**, 2662–2673, 2005.

Noh, Y., Cheon, W. G., Hong, S.-Y. and Raasch, S.: Improvement of the K-profile model for the planetary boundary layer based on large-eddy simulation data. *Bound.-Layer Meteor.*, **107**, 401–427, 2003.

Persing, J. and Montgomery, M. T.: Hurricane Superintensity. *J. Atmos. Sci.*, **60**, 2349–2371, 2003.

Pielke, R. A., Gratz, J., Landsea, C. W., Collins, D., Saunders, M. A., and Musulin, R.: Normalized Hurricane Damage in the United States: 1900–2005. *Natural Hazards Review*, **9**, 29–42, 2008.

Rotunno, R., Chen, Y., Wang, W., Davis, C., Dudhia, J., and Holland, G. J.: Large-Eddy Simulation of an Idealized Tropical Cyclone. *Bulletin of the American Meteorological Society*, **90**, 1783–1788, 2009.

Rotunno, R. and Bryan, G. H.: Effects of resolved turbulence in a large eddy simulation of a hurricane, paper presented at 31st Conference on Hurricanes and Tropical Meteorology, *Am. Meteorol. Soc.*, San Diego, Calif, 2014.

Smith, R. K. and Montgomery, M. T.: Hurricane boundary-layer theory. *Quarterly Journal of the Royal Meteorological Society*, **136**, 1665–1670, 2010.

Stern, D. P. and Bryan, G. H.: The structure and dynamics of coherent vortices in the eyewall boundary layer of tropical cyclones, paper presented at 31st Conference on Hurricanes and Tropical Meteorology, *Am. Meteorol. Soc.*, San Diego, Calif, 2014.

Stern, D. P., Bryan, G. H., and Aberson, S. D.: Extreme Low-Level Updrafts and Wind Speeds Measured by Dropsondes in Tropical Cyclones. *Monthly Weather Review*, **144**, 2177-2204, 2016.

Stern, D. P. and Bryan, G. H.: Using Simulated Dropsondes to Understand Extreme Updrafts and Wind Speeds in Tropical Cyclones. *Monthly Weather Review*, **146**, 3901-3925, 2018.

Wakimoto, R. M. and Black, P. G.: Damage Survey of Hurricane Andrew and Its Relationship to the Eyewall. *Bull. Amer. Meteor. Soc.*, **75**, 189–200, 1994.

Wurman, J. and Winslow, J.: Intense Sub-Kilometer-Scale Boundary Layer Rolls Observed in Hurricane Fran. *Science*, **280**, 555–557, 1998.

Wurman, J. and Kosiba, K.: The Role of Small-Scale vortices in Enhancing Surface Winds and Damage in Hurricane Harvey (2017). *Mon. Wea. Rev.*, **146**, 713-722, 2018.

Wu, L., Liu, Q., and Li, Y.: Prevalence of tornado-scale vortices in the tropical cyclone eyewall. *Proceedings of the National Academy of Sciences*, doi.org/10.1073/pnas.1807217115,2018.

Wu, L., Braun, S. A., Halverson, J., and Heymsfield, G.: A numerical study of Hurricane Erin (2001). Part I: Model verification and storm evolution. *J. Atmos. Sci.*, **63**, 65–86, 2006.

Wu, L. and Chen, X.: Revisiting the steering principle of tropical cyclone motion in a numerical experiment. *Atmos. Chem. Phys.*, **16**, 14925–14936, 2016.

Zhang, Q., Wu, L., and Liu, Q.: Tropical Cyclone Damages in China 1983–2006. *Bull. Amer. Meteor. Soc.*, **90**, 489–495, 2009.

Zhu, P.: Simulation and Parameterization of the Turbulent Transport in the Hurricane Boundary Layer by Large Eddies. *Journal of Geophysical Research*, **113**, D17104, 2008.

569 Zhu, P., Menelaou, K. and Zhu, Z.: Impact of Subgrid-Scale Vertical Turbulent Mixing
570 on Eyewall Asymmetric Structures and Mesovortices of Hurricanes: Impact of
571 SGS Vertical Turbulent Mixing on Eyewall Asymmetries. *Quarterly Journal of*
572 *the Royal Meteorological Society*, **140**, 416–438, 2013.

573

574

575

576

Table caption

Table 1 List of the identified tornado-scale vortices in the TCBL with the maximum updraft (m s^{-1}) and vertical relative vorticity (s^{-1}) and the corresponding altitudes (m) in the parentheses. The location column lists the radial distance from the TC center and the relative distance to the 500-m radius of maximum wind in the parentheses. The Richardson number (Ri) is averaged over the layer between 200-800 m within a radius of 1.5 km. The four strongest EVMs are indicated in bold.

Figure captions

Figure 1 Intensity of the simulated tropical cyclone during 24-36 h in terms of maximum instantaneous (red) and azimuthal-mean (blue) wind speeds at 10 m.

Figure 2 Simulated radar reflectivity (dBZ) at 500 m (a) and wind speed (m s^{-1}) at 10 m (b) within an area of 40×40 km^2 at 27 h. The plus signs and solid circles indicate the TC center and the radius of maximum wind at 500 m. The red dots indicate locations of tornado-scale vortices. The rectangle shows the area used in Fig. 3a. The arrow shows the vertical wind shear of 7.0 (27h) m s^{-1} between 200 hPa and 850 hPa.

Figure 3 (a) 10-m wind speed (m s^{-1}) and wind vectors and (b) the perturbation wind vectors and vertical component of relative vorticity (shading) at 500 m in the area shown in Fig. 2b. The straight line is the location of the vertical cross section in Figure 7 and M2701 and M2705 are the two tornado-scale vortices in the small area. The blue dots indicate their locations.

599 Figure 4 (a) Horizontal distribution of the tornado-scale vortices identified with the
600 thresholds of 15 m s^{-1} (yellow dots) and 20 m s^{-1} (red dots) in vertical motion
601 and the Richardson number (shading) averaged over 26-36 h; (b) the same as
602 (a), but for 27 h. The solid circle is the 500-m radius of maximum wind and
603 dashed circles indicate the distances from the TC center at 10-km intervals.

604 Figure 5 Radial-height cross sections of (a) tangential (shading) and radial (contour,
605 interval: 2 m s^{-1}) wind speeds, (b) upward motion (contour, interval: 0.5 m s^{-1})
606 and radar reflectivity (shading), and (c) tangential wind (contour, interval: 4 ms^{-1})
607 and the vertical component of relative vorticity (shading, unit: s^{-1}), which are
608 averaged over the northeastern quadrant during 26 h-36 h. The dots are the
609 locations of identified tornado-scale vortices. The dashed white lines indicate
610 the radius of maximum wind. The vertical and horizontal axes indicate the
611 altitude (km) from the surface and the relative distances (km) from the TC
612 center.

613 Figure 6 (a) The streamlines of the horizontal perturbation winds for M2701 and the
614 wind speed (shading) at the altitude of 10 m. (b) The nearly vertical slice of the
615 perturbation winds for M2701 with the red cycle indicating the
616 updraft/downdraft couplet. (c) The stream lines of the three dimensional
617 perturbation wind for M2701. The warm (cold) color of the streamline indicates
618 the upward (downward) vertical velocity perturbation and the vectors show the
619 near-surface wind fields. The vertical and horizontal axes indicate the altitude
620 (km) from the surface and the relative distances (km) from the nearest corner,
621 respectively.

622 Figure 7 The radial-height cross sections of the perturbation winds (vector) and (a)
623 vertical motion, (b) equivalent potential temperature, and (c) radar reflectivity
624 (shading) for M2701 along the line in Figure 3b. The abscissa indicates the
625 relative outward distance.

626 Figure 8 (a) The radial-height cross section of perturbation winds (vector) and
627 relative humidity (shading) for M2701, (b) the 400-m (blue) and 10-m (black)
628 wind speeds and the 400-m vertical relative vorticity for M2701 along the line
629 in Figure 3b. The abscissa indicates the relative outward distance.

630 Figure 9 The radial-height cross sections of the perturbation winds (vector) and (a)
631 vertical motion, (b) equivalent potential temperature for M2708, and (c) the
632 corresponding 900-m (blue) and 10-m (black) wind speeds. The abscissa
633 indicates the relative outward distance.

634 Figure 10 The radial-height cross sections of the perturbation winds (vector) and (a)
635 vertical motion, (b) equivalent potential temperature for M3002, and (c) the
636 corresponding 1300-m (blue) and 10-m (black) wind speeds. The abscissa
637 indicates the relative outward distance.

638

639

640 Table 2 List of the identified tornado-scale vortices in the TCBL with the maximum
641 updraft (m s^{-1}) and vertical relative vorticity (s^{-1}) and the corresponding altitudes (m) in
642 the parentheses. The location column lists the radial distance from the TC center and the
643 relative distance to the 500-m radius of maximum wind in the parentheses. The
644 Richardson number (Ri) is averaged over the layer between 200-800 m within a radius of
645 1.5 km. The four strongest EVMs are indicated in bold.

No.	**Updraft**	**Vorticity**	**Location**	**Ri**
M2600	22.75(800)	0.36(400)	23.6 (-5.5)	0.095
M2601	22.39(600)	0.23(500)	25.3 (-3.8)	0.111
M2700	27.37(500)	0.45(200)	25.6 (-3.0)	0.017
M2701	**31.98(400)**	**0.55(200)**	**24.3 (-4.3)**	**-0.008**
M2702	21.40(300)	0.30(300)	21.1 (-7.5)	0.029
M2703	20.46(400)	0.23(400)	27.9 (-0.7)	0.013
M2704	27.76(500)	0.34(400)	22.8 (-5.8)	0.032
M2705	22.26(600)	0.24(600)	27.9 (-0.7)	0.038
M2706	20.93(600)	0.23(500)	20.7 (-7.9)	-0.031
M2707	20.30(700)	0.21(700)	29.6 (1.0)	-0.011
M2708	22.20(900)	0.29(800)	31.2 (2.6)	-0.037
M2709	21.49(800)	0.22(800)	22.8 (-5.8)	0.052
M2800	20.12(400)	0.23(400)	27.0 (-1.7)	0.030
M2801	24.36(600)	0.39(400)	24.2 (-4.5)	-0.037
M2802	22.14(600)	0.30(500)	29.0 (0.3)	0.029
M2803	20.14(500)	0.23(500)	26.6 (-2.1)	0.025
M2900	**34.98(400)**	**0.48(200)**	**27.5 (-1.7)**	**0.042**
M2901	20.95(400)	0.21(400)	41.0 (11.8)	0.017
M3000	**35.77(400)**	**0.48(300)**	**28.1 (-0.1)**	**0.044**
M3001	**38.33(900)**	**0.49(400)**	**27.7 (-0.5)**	**0.067**
M3002	21.43(1300)	0.29(1300)	29.8 (1.6)	0.083
M3100	20.87(600)	0.24(700)	25.1 (-3.3)	-0.106
M3600	22.00(400)	0.35(400)	24.1 (-6.6)	0.146
M3601	22.68(600)	0.23(500)	38.0 (7.3)	-0.073

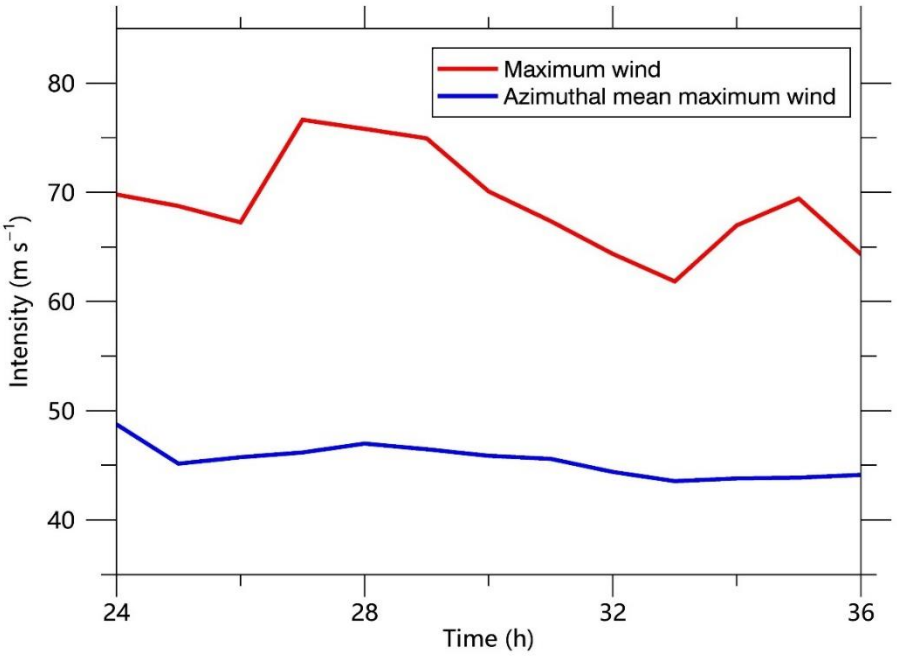

Figure 1 Intensity of the simulated tropical cyclone during 24-36 h in terms of maximum instantaneous (red) and azimuthal-mean (blue) wind speeds at 10 m.

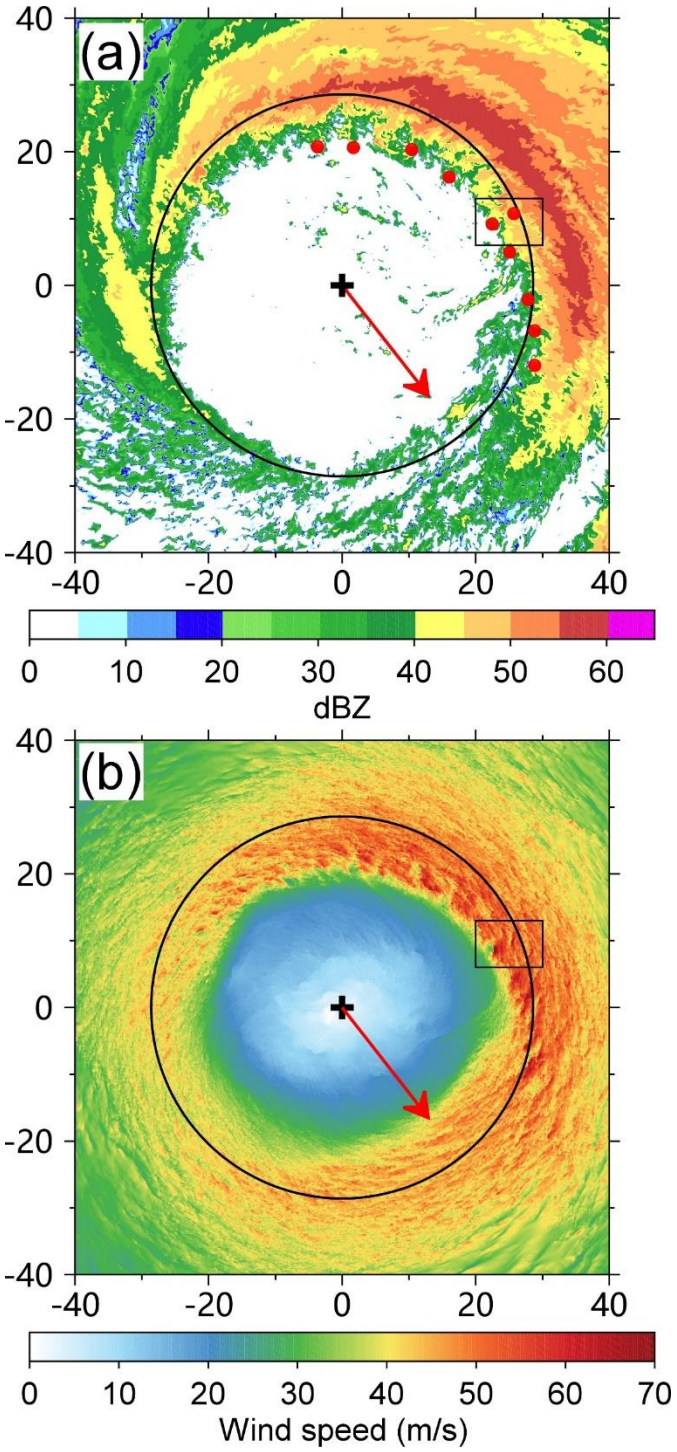

Figure 2 Simulated radar reflectivity (dBZ) at 500 m (a) and wind speed (m s^{-1}) at 10 m (b) within an area of 40×40 km^2 at 27 h. The plus signs and solid circles indicate the TC center and the radius of maximum wind at 500 m. The red dots indicate locations of tornado-scale vortices. The rectangle shows the area used in Fig. 3a. The arrow shows the vertical wind shear of 7.0 (27h) m s^{-1} between 200 hPa and 850 hPa.

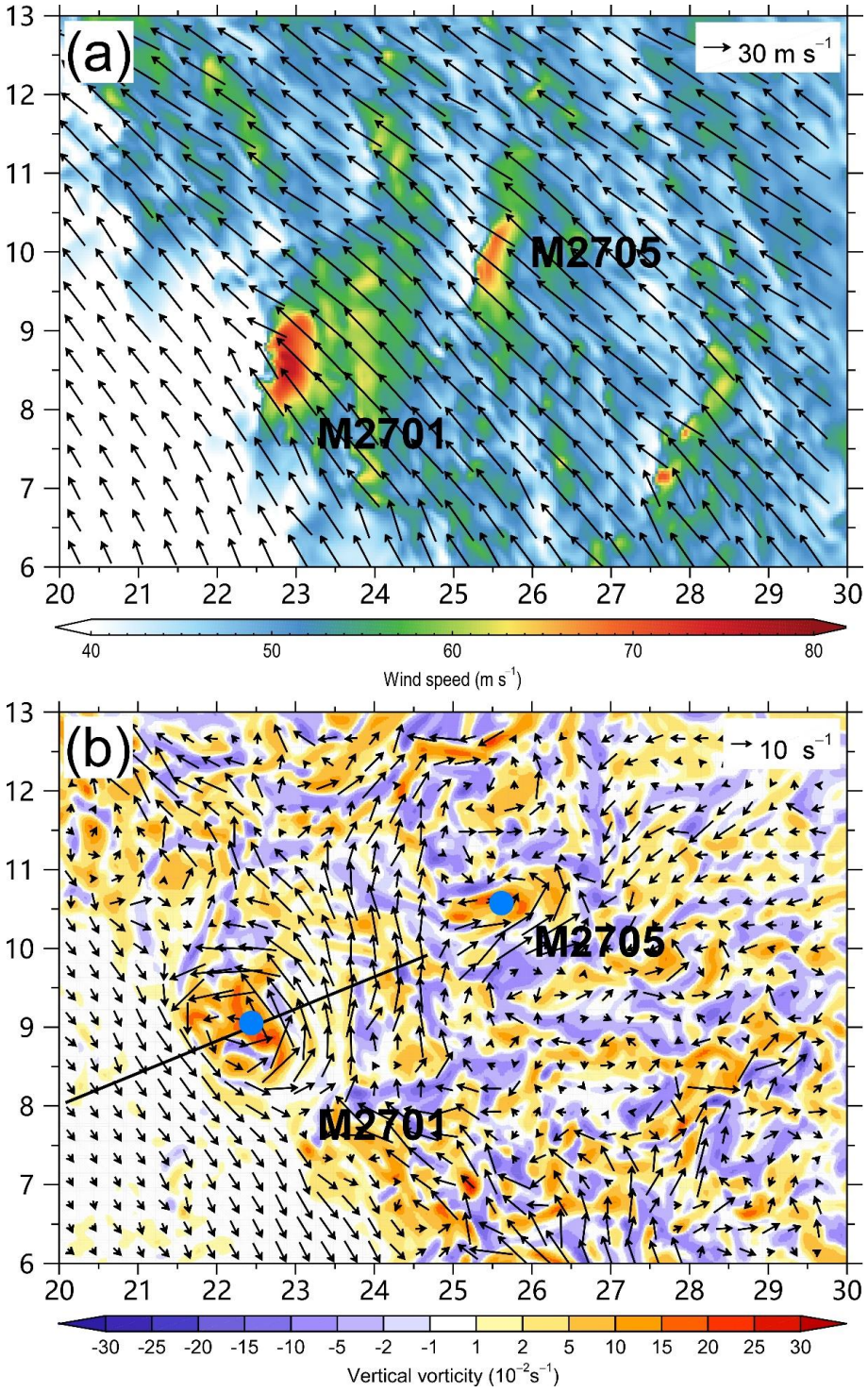

Figure 3 (a) 10-m wind speed (m s^{-1}) and wind vectors and (b) the perturbation wind vectors and vertical component of relative vorticity (shading) at 500 m in the area shown in Fig. 2b. The straight line is the location of the vertical cross section in Figure 7 and M2701 and M2705 are the two tornado-scale vortices in the small area. The blue dots indicate their locations.

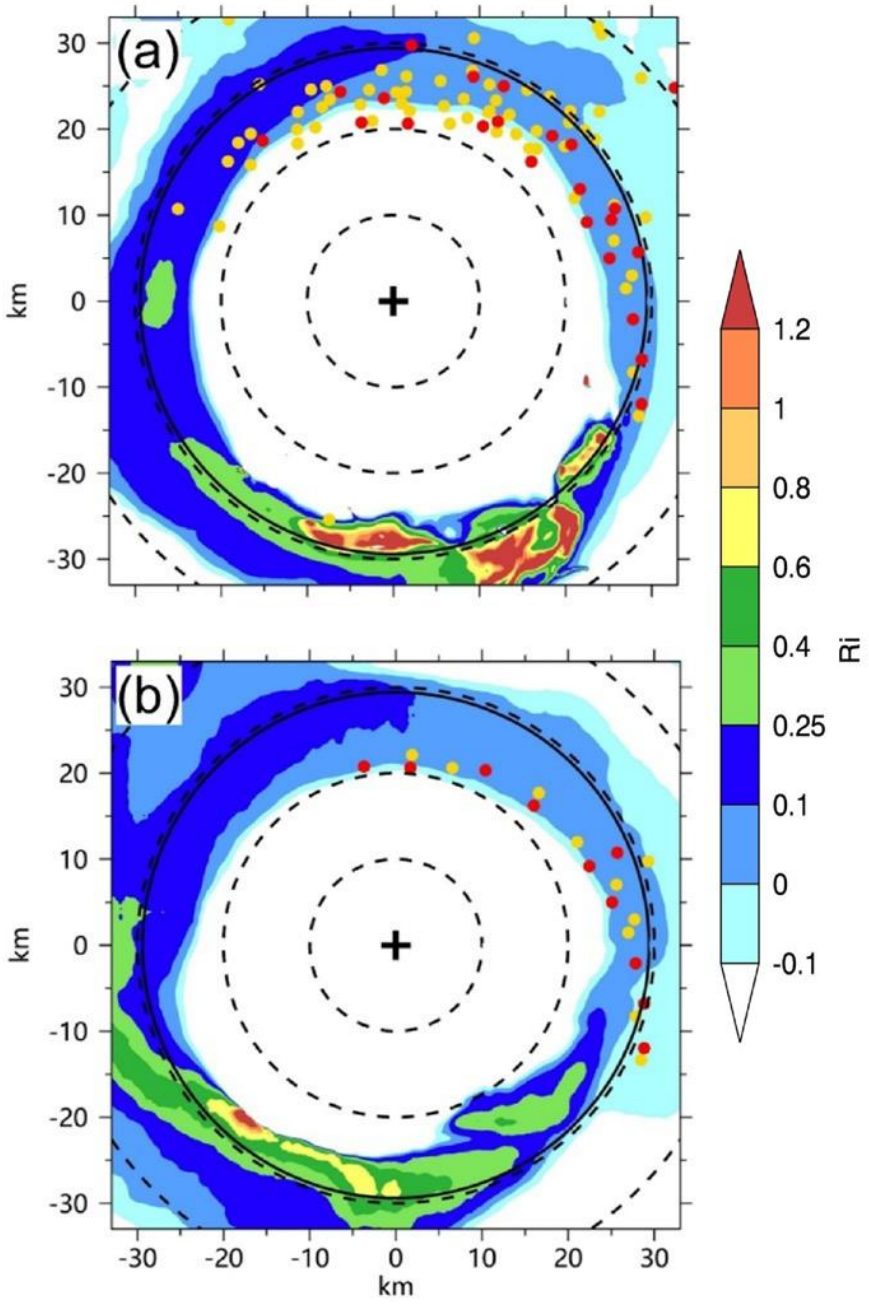

Figure 4 (a) Horizontal distribution of the tornado-scale vortices identified with the thresholds of 15 m s^{-1} (yellow dots) and 20 m s^{-1} (red dots) in vertical motion and the Richardson number (shading) averaged over 26-36 h; (b) the same as (a), but for 27 h. The solid circle is the 500-m radius of maximum wind and dashed circles indicate the distances from the TC center at 10-km intervals.

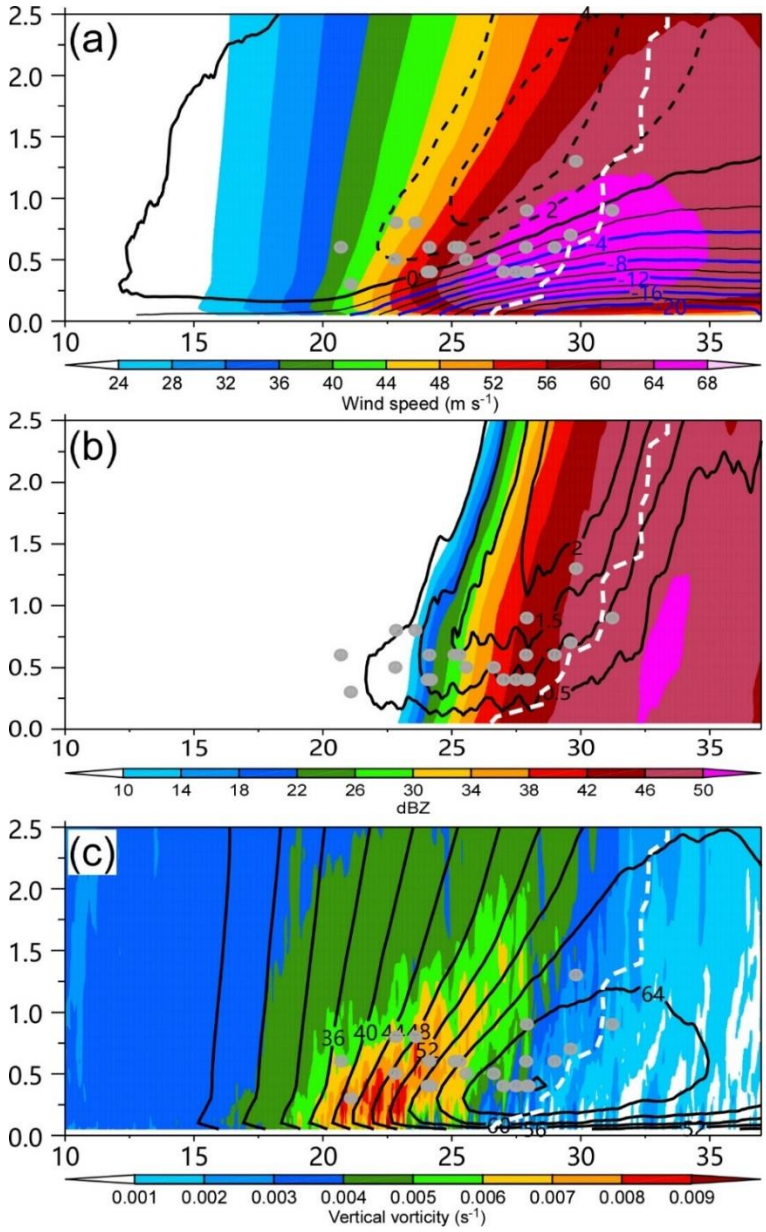

669

670 Figure 5 Radial-height cross sections of (a) tangential (shading) and radial (contour,
671 interval: 2 m s^{-1}) wind speeds, (b) upward motion (contour, interval: 0.5 m s^{-1}) and radar
672 reflectivity (shading), and (c) tangential wind (contour, interval: 4 ms^{-1}) and the vertical
673 component of relative vorticity (shading, unit: s^{-1}), which are averaged over the
674 northeastern quadrant during 26 h-36 h. The dots are the locations of identified tornado-
675 scale vortices. The dashed white lines indicate the radius of maximum wind. The vertical
676 and horizontal axes indicate the altitude (km) from the surface and the relative distances
677 (km) from the TC center.

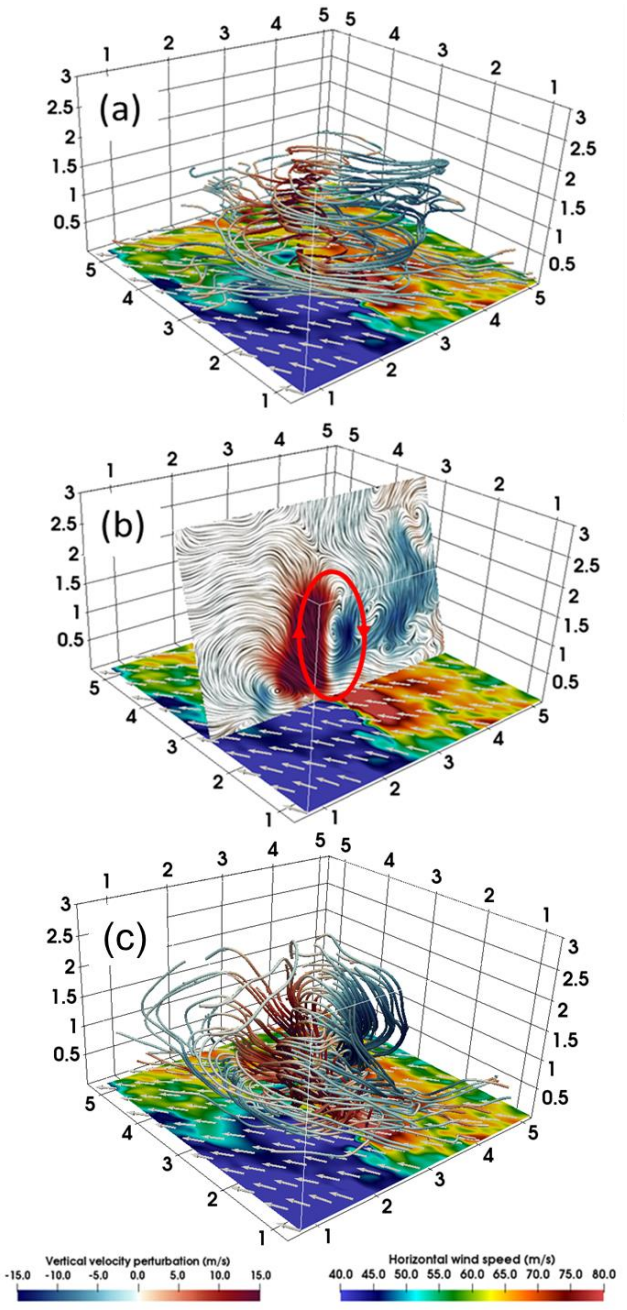

Figure 6 (a) The streamlines of the horizontal perturbation winds for M2701 and the wind speed (shading) at the altitude of 10 m. (b) The nearly vertical slice of the perturbation winds for M2701 with the red cycle indicating the updraft/downdraft couplet. (c) The stream lines of the three dimensional perturbation wind for M2701. The warm (cold) color of the streamline indicates the upward (downward) vertical velocity perturbation and the vectors show the near-surface wind fields. The vertical and horizontal axes indicate the altitude (km) from the surface and the relative distances (km) from the nearest corner, respectively.

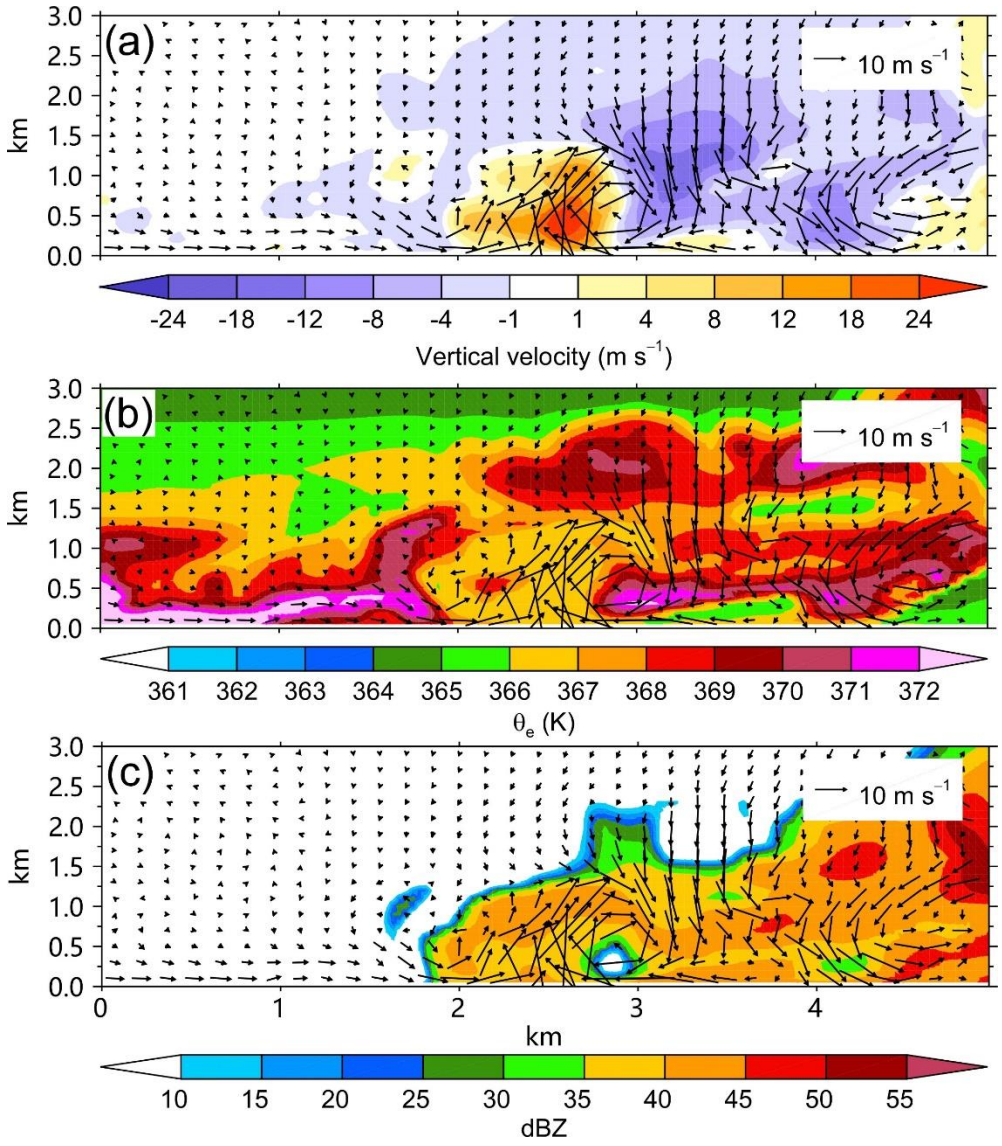

687

688 Figure 7 The radial-height cross sections of the perturbation winds (vector) and (a)
689 vertical motion, (b) equivalent potential temperature, and (c) radar reflectivity (shading)
690 for M2701 along the line in Figure 3b. The abscissa indicates the relative outward
691 distance.

692

693

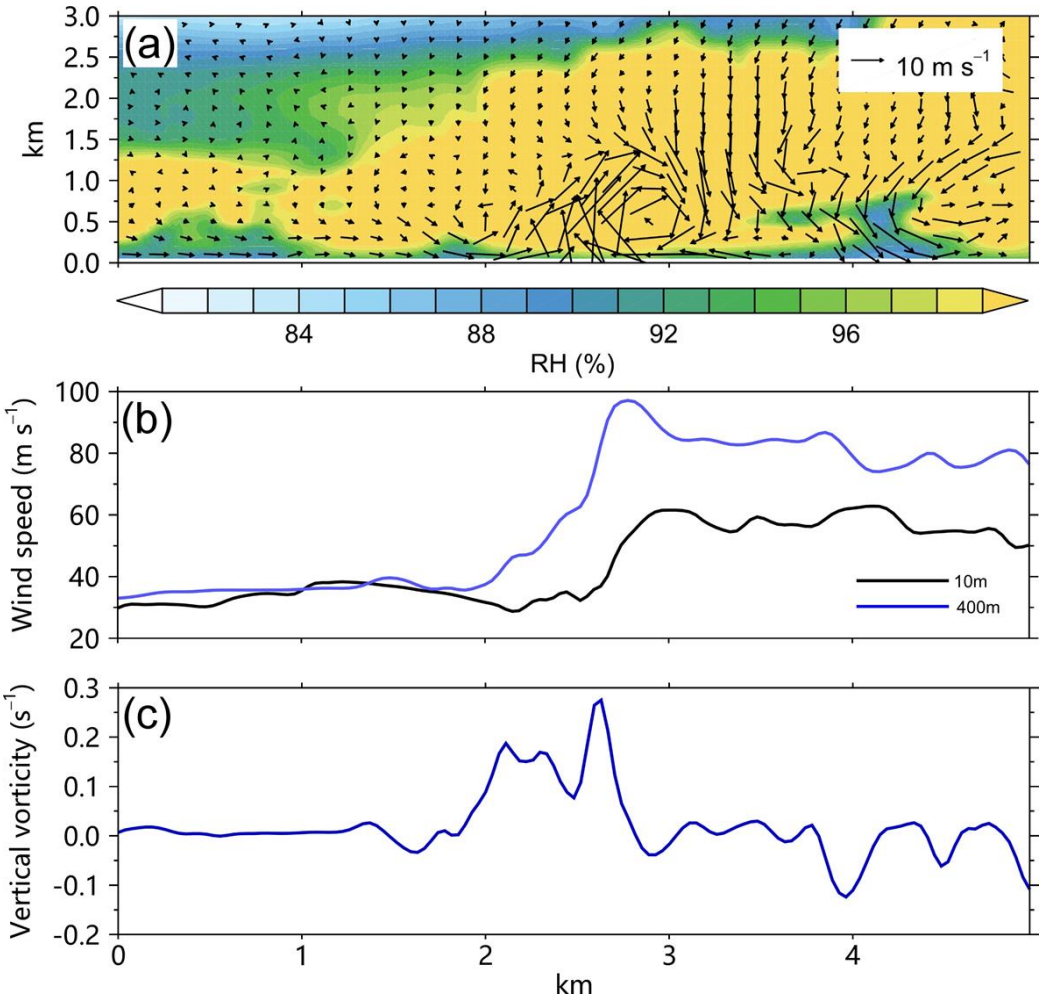

694

695 Figure 8 (a) The radial-height cross section of perturbation winds (vector) and relative
696 humidity (shading) for M2701, (b) the 400-m (blue) and 10-m (black) wind speeds and
697 the 400-m vertical relative vorticity for M2701 along the line in Figure 3b. The abscissa
698 indicates the relative outward distance.

699

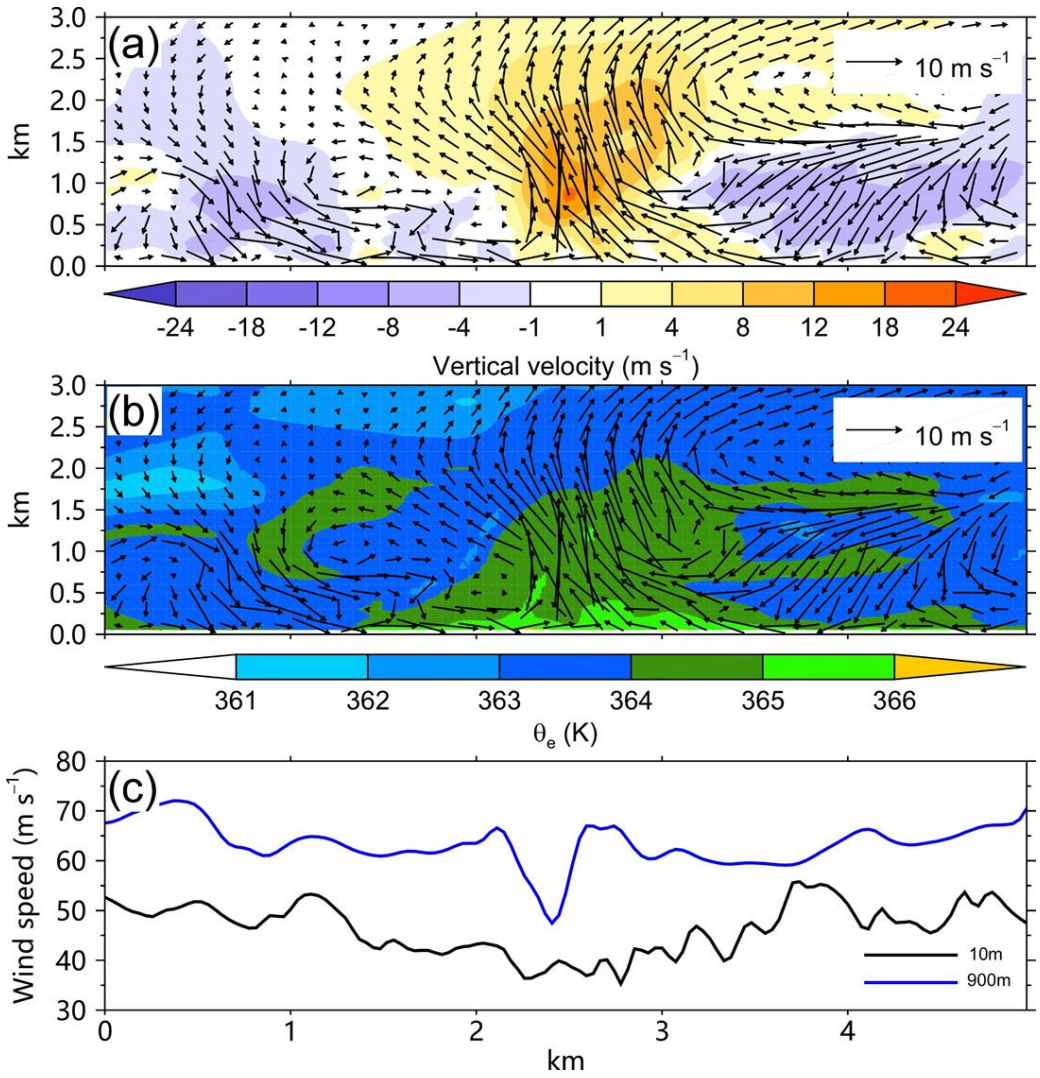

Figure 9 The radial-height cross sections of the perturbation winds (vector) and (a) vertical motion, (b) equivalent potential temperature for M2708, and (c) the corresponding 900-m (blue) and 10-m (black) wind speeds. The abscissa indicates the relative outward distance.

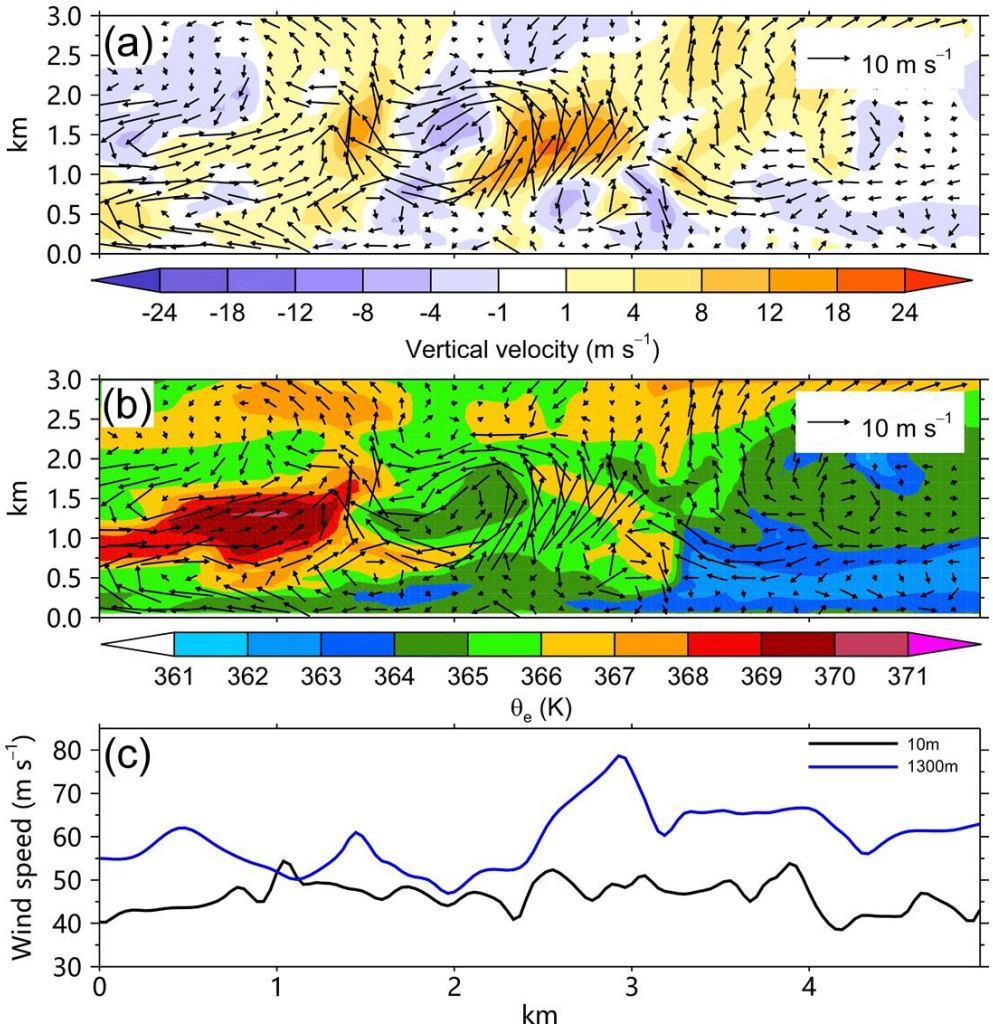

Figure 10 The radial-height cross sections of the perturbation winds (vector) and (a) vertical motion, (b) equivalent potential temperature for M3002, and (c) the corresponding 1300-m (blue) and 10-m (black) wind speeds. The abscissa indicates the relative outward distance.